

Article

# Preparation and Photocatalytic Properties of Heterostructured Ceria/Polyaniline Nanoparticles

Yen-Sheng Li <sup>1</sup>, Alex Fang <sup>2</sup>, Gang-Juan Lee <sup>3</sup>, Jerry J. Wu <sup>3</sup>, Yu-Cheng Chang <sup>1</sup>, Chien-Yie Tsay <sup>1</sup> ,  
Jing-Heng Chen <sup>4</sup>, Tzyy-Leng Horng <sup>5</sup> and Chin-Yi Chen <sup>1,2,\*</sup> 

<sup>1</sup> Department of Materials Science and Engineering, Feng Chia University, Taichung 407, Taiwan; show41406@gmail.com (Y.-S.L.); yuchchang@fcu.edu.tw (Y.-C.C.); cytsay@fcu.edu.tw (C.-Y.T.)

<sup>2</sup> Department of Engineering Technology and Industrial Distribution, Texas A&M University, College Station, TX 77843, USA; gpafang@tamu.edu

<sup>3</sup> Department of Environmental Engineering and Science, Feng Chia University, Taichung 407, Taiwan; leeganjuan@gmail.com (G.-J.L.); jjwu@mail.fcu.edu.tw (J.J.W.)

<sup>4</sup> Department of Photonics, Feng Chia University, Taichung 407, Taiwan; jhchen@fcu.edu.tw

<sup>5</sup> Department of Applied Mathematics, Feng Chia University, Taichung 407, Taiwan; tlhorng123@gmail.com

\* Correspondence: chencyi@fcu.edu.tw

Received: 3 June 2020; Accepted: 30 June 2020; Published: 2 July 2020



**Abstract:** Cerium dioxide (CeO<sub>2</sub>, ceria), a promising and abundant catalytic material with high-efficiency, nontoxicity, photochemical stability, and affordability, can be used as a photocatalyst to photocatalytically degrade organics and split water for hydrogen production under ultraviolet (UV) irradiation (about 5% of solar energy). However, the applications of the CeO<sub>2</sub> photocatalyst are limited due to low photocatalytic efficiency under sunlight irradiation. In this study, a nanosized CeO<sub>2</sub> powder was prepared by the precipitation method. Subsequently, various amounts of polyaniline (PANI) nanoparticles were deposited onto the surface of the CeO<sub>2</sub> nanoparticles to form a heterostructure by the polymerization method. The crystal structure, morphology, surface and optical properties of the CeO<sub>2</sub>/PANI nanoparticles were investigated by X-ray diffractometry (XRD), scanning electron microscopy (SEM), Fourier-transform infrared spectroscopy (FTIR), ultraviolet-visible (UV-Vis) absorption spectroscopy, and photoluminescence (PL). Experimental results demonstrated that PANI deposition improved the light absorption of CeO<sub>2</sub> nanoparticles in the visible light region. The heterostructured CeO<sub>2</sub>/PANI nanoparticle with 4 wt % PANI deposition exhibited optimal photocatalytic activities with a hydrogen production rate of 462 μmolg<sup>-1</sup> within 6 h and a methyl orange (MO) degradation rate of 45% within 4 h under visible light irradiation. The photocatalytic mechanisms of the composite powder are also proposed in this report.

**Keywords:** polyaniline; cerium dioxide; heterostructured powder; photocatalyst; precipitation

## 1. Introduction

With the increasing depletion of fossil fuels, such as coal, oil, and natural gas, the search for alternative and renewable energy sources has become a top priority. The use of solar energy, a clean primary energy source with high efficiency and low energy exhaust, is crucially important [1]. Hydrogen is a colorless, odorless, and non-toxic flammable gas energy source, and is also the most abundant element in nature. Hydrogen forms various chemical components with other elements. As the final product of the compounds formed by hydrogen and oxygen is water, using hydrogen as a clean energy source does not pollute the environment. To date, hydrogen production technologies include thermochemical, water electrolysis, biological and photocatalytic processes, etc. [2]. Among them, the photocatalytic method possesses the advantages of low cost, no pollution, high cycle stability,

and when used in conjunction with solar energy, has attracted particular attention and become one of the popular promising energy-related research topics [3,4].

Numerous researchers have long worked to develop materials that can be combined or compatible with nature. As a material of green technology, the semiconductor photocatalyst has received extensive attention in related fields for its highly efficient decomposition of toxic compounds, bacteria, and other pollutants, as well as for its water splitting ability to produce hydrogen gas [4,5]. Among the photocatalytic materials, titanium dioxide ( $\text{TiO}_2$ ) is the earliest and most widely used photocatalyst due to its high photocatalytic activity, non-toxicity, low cost, and excellent physiochemical stability [6–8]. Compared with  $\text{TiO}_2$ , cerium oxide (ceria,  $\text{CeO}_2$ ) with two valence states  $\text{Ce}^{4+}$  and  $\text{Ce}^{3+}$  has better catalytic activity in the near ultraviolet or ultraviolet light region [9] and is abundant in the earth's crust, thus lending itself as a strong economical contender [10]. Therefore, much effort has been made to study and to further improve the photocatalytic activity of  $\text{CeO}_2$  [11]. In spite of knowing that  $\text{CeO}_2$  exhibits the ability to photocatalytically split water into hydrogen and oxygen, a drawback of the photocatalytic process is that it must be excited in the ultraviolet (UV) light irradiation by a light wavelength less than 388 nm [12]. That is to say, lower than ~5% intensity in solar energy can be used, but not the visible light and infrared light regions [13]. Therefore, in the past ten years, there have been many studies dedicated to improving the catalytic activity of cerium oxide under visible light [14] by means of changing the morphology [15], modification with noble metals [16,17], co-catalyst loading [18–20], and aliovalent doping [21,22], etc.

Polyaniline (PANI), an intrinsically conducting polymer (ICP), possessing the advantages of adjustable electrical conductivity, excellent environmental stability, affordability, and ease of synthesis, has been applied to many research fields, such as supercapacitors, sensors and batteries [23–27]. Recently, PANI has been studied to coordinate with metal oxides to form nanostructured composites for photocatalyst applications due to its wide absorption region in the visible light range [28–31]. It has been demonstrated that PANI in hybrid materials can experience changes in morphology, optical properties, and electrical conductivity [32,33], which may improve the photocatalytic performance of nanocomposites [34,35]. However, to date, although there have been studies that have reported the synthesis of PANI/ $\text{CeO}_2$  nanocomposite [36] or investigated the characteristics of its photocatalytic degradation of organics [37,38], the precipitated  $\text{CeO}_2$  nanoparticle has not been directly coated with various amounts of PANI for the investigation of the photocatalytic degradation and water splitting performance. In the present novel study,  $\text{CeO}_2$  powders with an extremely small particle size were synthesized from cerium nitrate by precipitation; subsequently, various amounts of PANI were directly deposited onto the surface of the  $\text{CeO}_2$  particle for the fabrication of heterostructured  $\text{CeO}_2$ /PANI photocatalysts by polymerization. The structural and morphological properties as well as the photocatalytic performance, including organics degradation and water splitting of the  $\text{CeO}_2$ /PANI powder, was investigated under visible light irradiation as a function of PANI deposition.

## 2. Results and Discussion

The phase identification and crystal structure of the material can be performed by XRD analysis. Figure 1 shows the XRD patterns of the  $\text{CeO}_2$ /PANI composite powders as a function of the amount of PANI coating. Note that both the as-synthesized  $\text{CeO}_2$  powder and the samples with PANI conformed to JCPSD 34-0394, showing a cubic fluorite structure, which is consistent with the literature [39]. No significant shift in diffraction peaks of the  $\text{CeO}_2$  powder can be found after coating PANI, showing that the polymerization of PANI did not cause a change in the lattice of  $\text{CeO}_2$ . Moreover, no diffraction peaks of PANI were found in any of the  $\text{CeO}_2$ /PANI composite powders. It is likely due to the low crystallinity and low concentration of the coated PANI. The presence of PANI will be further verified by FTIR analysis.

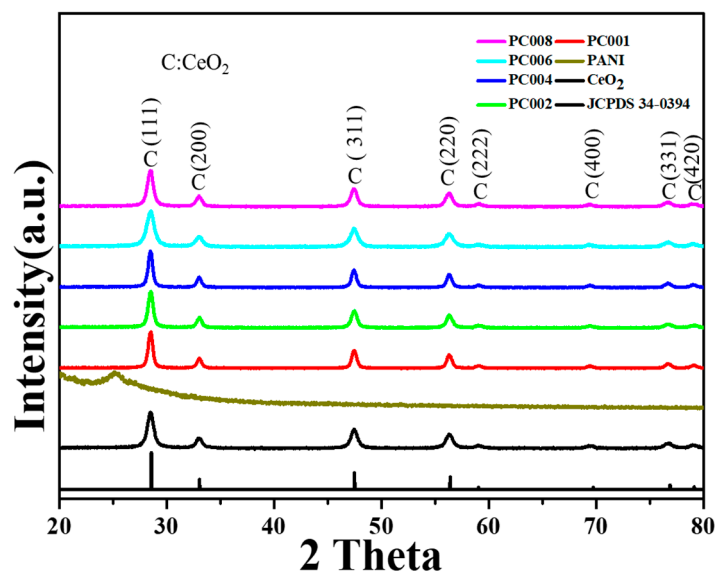


**Figure 1.** XRD pattern of the CeO<sub>2</sub>/PANI powders as a function of the amount of PANI coating.

The surface morphology of the composite powders can be observed by FE-SEM analysis. Figure 2 shows the SEM images of the CeO<sub>2</sub>/PANI powder as a function of coated PANI concentration. As shown in Figure 2a, the CeO<sub>2</sub> powder prepared by the precipitation method was rounded in shape and exhibited a particle size distribution in the range of 20–30 nm. However, the particle size increased after a small amount of PANI was coated. Subsequently, it showed a tendency of agglomeration as the PANI coating increased by more than 4 wt %. In order to determine the particle size distribution more clearly, TEM results are shown for further analysis.

To further understand the characteristics of the photocatalytic powder, Table 1 lists the specific surface area, particle size, and crystallite size of CeO<sub>2</sub>/PANI powders as a function of the amount of PANI coating. Note that the uncoated CeO<sub>2</sub> powder exhibited the largest specific surface area of 52.1 m<sup>2</sup>/g, then the value decreased dramatically as the PANI was deposited. This can be attributed to the PANI covering most of the surface of CeO<sub>2</sub> particles, thereby causing the decrease in surface area of the composite powders. Moreover, the particle size measured from the SEM images (more than 200 particles were taken) indicated that the composite powders exhibited a CeO<sub>2</sub> particle size range of ca. 20–40 nm. A significant increase in CeO<sub>2</sub> particle size can be noted when a small amount of PANI was deposited. This is most likely due to the growth of CeO<sub>2</sub> particles inter-diffusing at a relatively short distance during polymerization of a small amount of aniline. Similarly, such effect can also be found from the crystallite size results of the composite powder, as listed in Table 1, where the crystallite size was estimated from the XRD peak broadening using the Scherrer's formula. When the amount of PANI deposition increased above 4 wt %, the excess amorphous phase of PANI tended to transform the effect to cause the agglomeration of CeO<sub>2</sub> particles.

**Table 1.** Specific surface area (BET (Brunauer-Emmer-Teller) surface area), particle size and crystallite size of CeO<sub>2</sub>/PANI powders as a function of the amount of PANI deposition.

Sample	CeO <sub>2</sub>	PC001	PC002	PC004	PC006	PC008
BET surface area (m <sup>2</sup> /g)	52.1	30.0	16.2	20.6	21.4	26.1
Particle size (nm)	23.6	37.6	36.4	28.5	34.3	32.8
Crystallite size (nm)	13.3	15.4	14.2	16.0	9.9	12.0

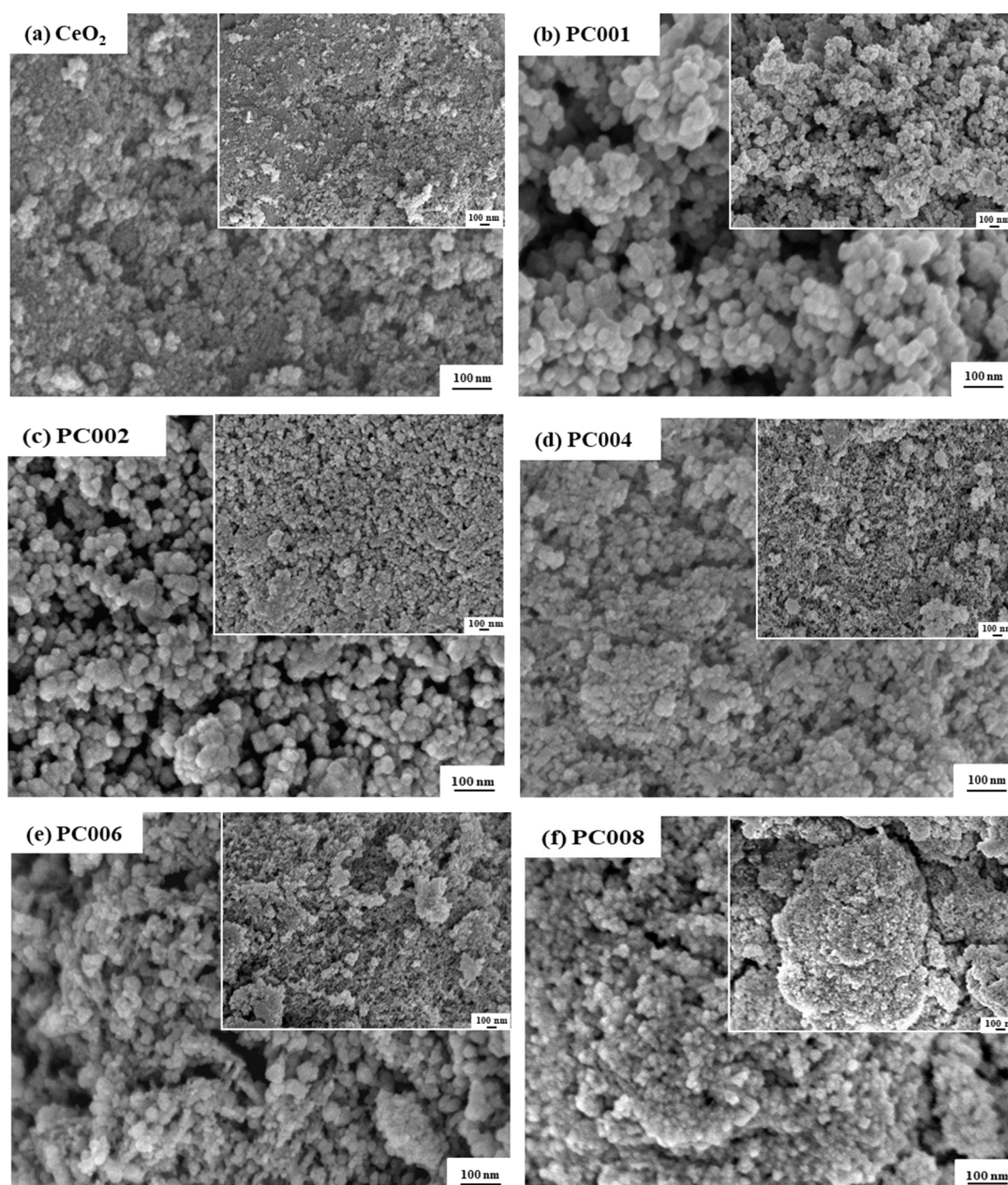


**Figure 2.** SEM micrographs of the CeO<sub>2</sub>/PANI powders as a function of coated PANI concentration.

Figure 3 shows the TEM images of the CeO<sub>2</sub> powder without and with PANI coating. The selected area diffraction (SAED) pattern of CeO<sub>2</sub> powder is also shown in this figure (Figure 3c). Note in Figure 3a that the plain CeO<sub>2</sub> powder (without PANI coating) exhibited a mean particle size of ca. 20 nm, as consistent with the FE-SEM results. In Figure 3b, the high-resolution TEM (HR-TEM) image of the CeO<sub>2</sub> powder, the lattice fringes of two or more different directions show that CeO<sub>2</sub> prepared by the precipitation method exhibit a CeO<sub>2</sub> cubic phase with a polycrystalline structure. Moreover, the interplanar spacing of the (111) plane is 0.31 nm, while the interplanar spacing of the (200) plane is 0.27 nm, being confirmed as a cubic CeO<sub>2</sub> structure, as consistent with the results in the literature [40,41]. Additionally, several dotted diffraction rings can be observed in the SAED pattern, Figure 3c, identifying the nanocrystalline structure of the CeO<sub>2</sub> powder. The diffraction patterns of CeO<sub>2</sub> for (111), (200), (311), and (220) planes were observed to agree with the XRD analysis. In Figure 3d, the TEM image of PC004, PANI was observed to be successfully coated onto the surface of the CeO<sub>2</sub> particle, the translucent film indicated by the arrow, thereby increasing the CeO<sub>2</sub> particle

size distribution to 25–40 nm. Meanwhile, the coated PANI tended to cause agglomeration of the CeO<sub>2</sub> powder.

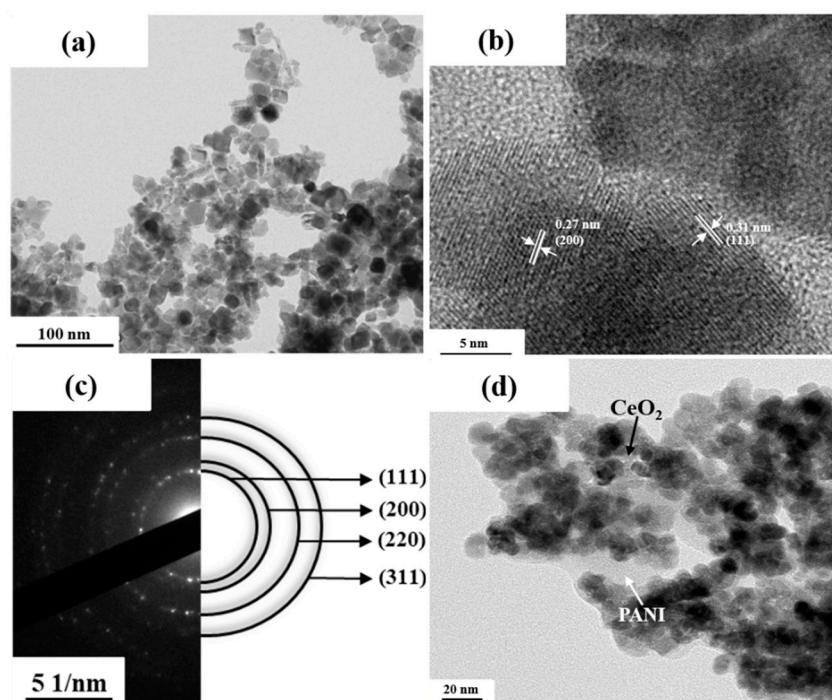


**Figure 3.** (a) TEM image, (b) HR-TEM lattice fringe image and (c) SAED pattern of the uncoated CeO<sub>2</sub> powder synthesized by precipitation. (d) TEM image of the 4 wt % PANI-coated CeO<sub>2</sub> powder (PC004).

FTIR can be used to determine the functional group and intramolecular bonding of the material. Figure 4 shows the FTIR spectra of the CeO<sub>2</sub>/PANI powders as a function of the amount of PANI coating. Unlike the spectrum of the uncoated CeO<sub>2</sub> powder, the FTIR spectra of the PANI coated CeO<sub>2</sub> was almost identical to that of PANI reported in the literature [42–45]. Note that in the patterns of CeO<sub>2</sub> with PANI coating, the presence of a band at ca. 818 cm<sup>-1</sup> was attributed to the out-of-plane deformation of C–H in a benzene ring [42,43]. The peak observed at ca. 1107 cm<sup>-1</sup> was the characteristic band of the stretching vibration of quinoid, while the band at ca. 1296 cm<sup>-1</sup> was associated with the C–N stretching vibrations of benzenoid rings of PANI [44]. The two bands at ca. 1580 and 1510 cm<sup>-1</sup> were assigned to the C=N and C=C stretching vibrations of the quinoid and benzenoid rings, respectively [45]. Altogether, this indicates that the PANI was successfully synthesized on the surface of the CeO<sub>2</sub> powder.

Figure 5 shows the UV-Vis curves of the CeO<sub>2</sub>/PANI powder as a function of coated PANI concentration. Note that the plain CeO<sub>2</sub> powder predominantly absorbs ultraviolet light to form electron-hole pairs in the wavelength range of <400 nm due to its large energy band gap, showing almost no absorption in the wavelength region of visible light (400–700 nm). In contrast, the samples with PANI coating all showed an improvement in the absorption of visible light. Among them, 4 wt % PANI-coated CeO<sub>2</sub> powder exhibited the best visible light absorption capacity, demonstrating that the light absorption range of CeO<sub>2</sub> can be extended to the visible light region by coating with PANI, thereby improving the photocatalytic activity. When the amount of PANI coating increased to 6–8 wt %, the light absorption capacity regressed, likely due to the formation of particle agglomeration from an excessive coating of PANI, causing a reduction in the visible light absorption capacity.

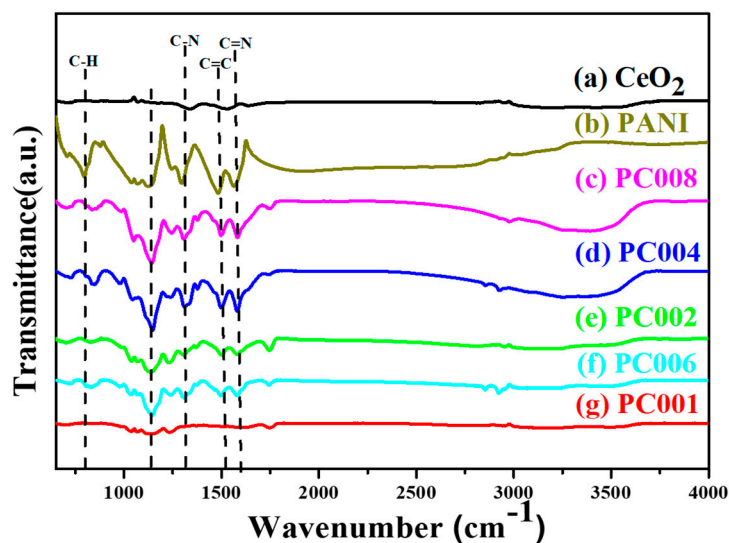


Figure 4. FTIR spectrum of the CeO<sub>2</sub>/PANI powders as a function of the amount of PANI coating.

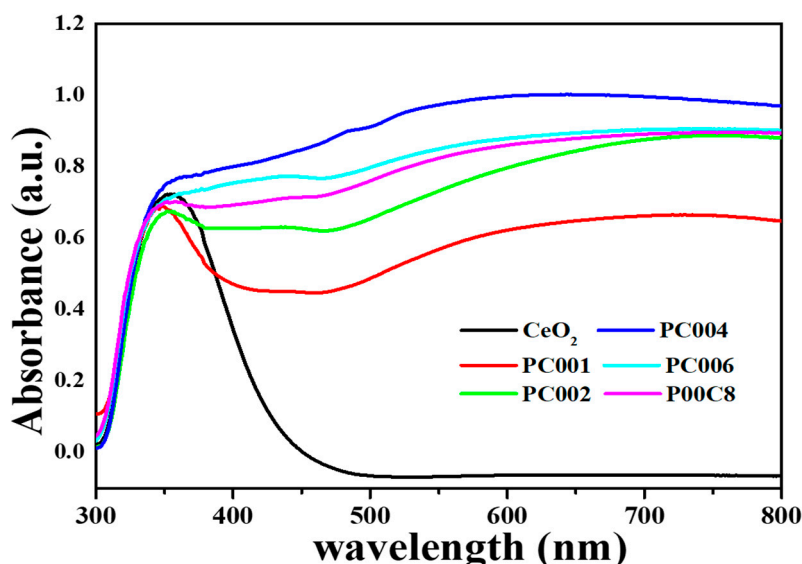


Figure 5. UV-Vis curve of the CeO<sub>2</sub>/PANI powders as a function of the amount of PANI coating.

Figure 6 shows the PL spectra of the CeO<sub>2</sub>/PANI powder as a function of the amount of PANI coating. Photo-induced fluorescence spectroscopy can be used to determine and obtain a comparison of the energy released by electron-hole pair recombination in semiconductors. Note that the plain CeO<sub>2</sub> powder exhibited the highest PL intensity, indicating that it had the highest recombination rate of photo-generated electron-hole pairs. In contrast, the PL intensity of the CeO<sub>2</sub> powders coated with PANI was significantly reduced. The inset shows the enlarged view of the red circle in Figure 6. The PL peak intensity gradually decreased with the increase in the amount of PANI coating. In addition to the fact that PANI itself is known to generate electron-hole pairs under visible light irradiation, this suggests that the PANI coating can effectively enhance the separation of photo-generated electron-hole pairs of composite powder, prolong the recombination time, and improve its photocatalytic activity.

In the hydrogen production test, the sacrificial reagents such as sulfites [41,46,47] and alcohols [48] are most commonly used to enhance the hydrogen production efficiency of a photocatalyst. In this study, sodium sulfite (Na<sub>2</sub>SO<sub>3</sub>) was confirmed to be used as the sacrificial reagent to increase the hydrogen production efficiency by 6.5 times (462.8/70.9) compared to the absence of Na<sub>2</sub>SO<sub>3</sub>, as shown in Figure 7a. It is generally believed that Na<sub>2</sub>SO<sub>3</sub>, as a strong oxidant, generates electrons after being

excited by light irradiation, which can effectively combine with holes in semiconductor photocatalyst materials. This enables the electron-hole pairs in the photocatalyst to be more effectively separated and to avoid their recombination, thereby further enhancing the photocatalytic activity. Furthermore, Figure 7b shows the hydrogen production efficiency of the PC004 after 6 h of visible light irradiation as a function of catalyst powder loading. Note that the hydrogen production efficiency of the PC004 increased with the increase in catalyst loading to 0.1 g/L as a result of the larger surface area providing more active sites for photocatalytic reaction. However, when the catalyst loading was increased to 0.15 mg/L, the hydrogen production efficiency of the PC004 decreased. This is most likely attributed to the high concentration of the catalyst inhibiting the light from entering the solution. The reduction in visible light absorption reduced the photocatalytic activity of the catalyst.

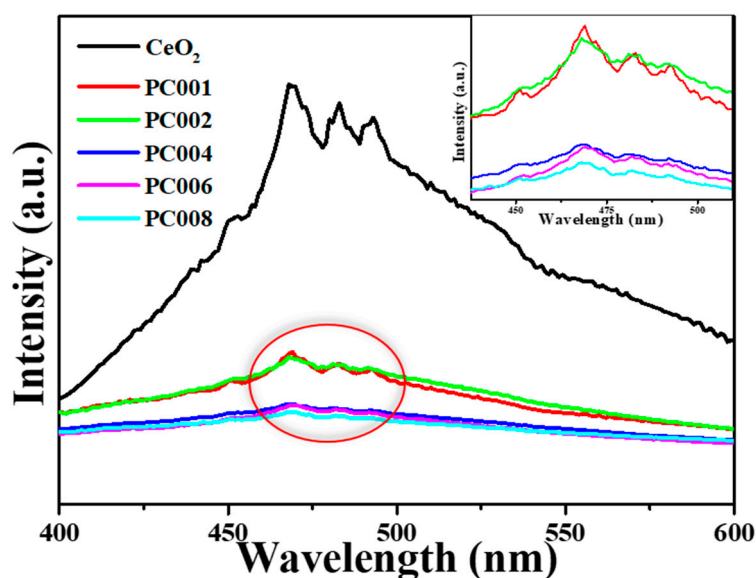


Figure 6. PL spectrum of the CeO<sub>2</sub>/PANI powders as a function of the amount of PANI coating.

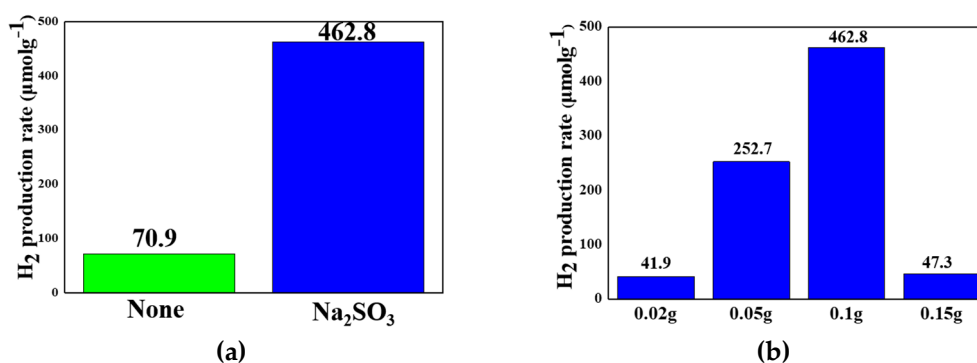
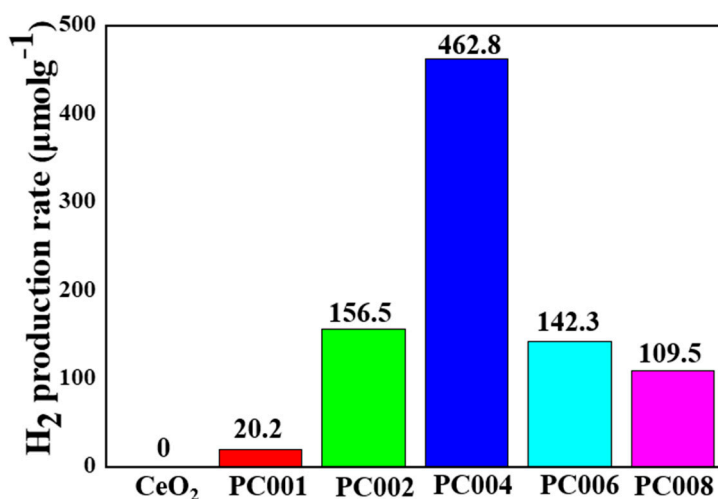


Figure 7. Hydrogen production efficiency of the PC004 (a) without and with Na<sub>2</sub>SO<sub>3</sub> addition, and (b) as a function of catalyst powder loading after 6 h of visible light irradiation.

It has been demonstrated that the separation of photogenerated electron-hole pairs can be effectively enhanced due to the formation of a heterostructure, the so-called *p-n* junction, at the interface between *n*-type CeO<sub>2</sub> and *p*-type PANI [49,50]. Figure 8 shows the comparison of the hydrogen production activity by photocatalytic water splitting of the heterostructured CeO<sub>2</sub>/PANI powder as a function of the amount of PANI coating after 6 h of visible light irradiation. Note that the uncoated CeO<sub>2</sub> powder exhibited no activity of hydrogen production after 6 h of irradiation. That is to say the CeO<sub>2</sub> powder has no photocatalytic activity under visible light irradiation. This implies that the CeO<sub>2</sub> with a large energy band gap, which cannot be excited by visible light irradiation, can only

produce hydrogen under UV light. Compared to the unaltered form, the CeO<sub>2</sub> powder showed better photocatalytic hydrogen production after adding PANI. Among them, the PC004 exhibited the highest hydrogen production efficiency, attaining a value of 462.8 μmolg<sup>-1</sup> after 6 h of visible light irradiation. The increase in photocatalytic activity can be attributed to the deposition of PANI, which can enhance the absorption of energy in the visible light region and facilitate the separation of photo-generated electron-hole pairs while inhibiting the rate of their recombination. However, when increasing the amount of PANI added to 6 wt % (PC006 and PC008), the hydrogen production effect began to decrease. It is speculated that the main reason for this is that the excessive addition of PANI caused agglomeration on the surface of the CeO<sub>2</sub> powder during the preparation process, which tends to reduce the active sites of the reaction and thus decreased the photocatalytic activity.



**Figure 8.** Hydrogen production efficiency by photocatalytic water splitting of the heterostructured CeO<sub>2</sub>/PANI powders as a function of the amount of PANI coating after 6 h of visible light irradiation.

The photocatalytic performance of the heterostructured CeO<sub>2</sub>/PANI powders was also evaluated by degrading the methylene orange (MO) under visible light irradiation. Figure 9 shows the MO photodegradation curves of the CeO<sub>2</sub>/PANI composite powders under visible light irradiation as a function of the amount of PANI coating. However, physical adsorption may occur during the process. All degradation curves of the composite powders under visible light irradiation are thus presented after deducting the physical adsorption effect by a 30-min dark adsorption before illumination. It should be noted that, without photocatalyst, MO degradation was confirmed to be negligible under visible light irradiation, see the “blank” curve. Similarly, no degradation effect of the uncoated CeO<sub>2</sub> powder can be found under visible light irradiation due to its large energy band gap (~3.2 eV) which can only be activated by UV light. Compared with the uncoated CeO<sub>2</sub> and PANI powders, the photodegradation effect of all samples coated with PANI is improved. Note that the highest photocatalytic activity is shown by the CeO<sub>2</sub> powder coated with 4 wt % PANI; exhibiting a MO photodegradation of 45.1% after 4 h of visible light irradiation. Similar synergistic effects can also be found in other composite systems of PANI/BiOI [50], PANI/BiOBr [51] and PANI/BiOCl [31]. This can be attributed to the presence of PANI, which increases the photogenerated electron-hole separation and inhibits the recombination rate, thereby improving the photocatalytic activity of the CeO<sub>2</sub> powder.

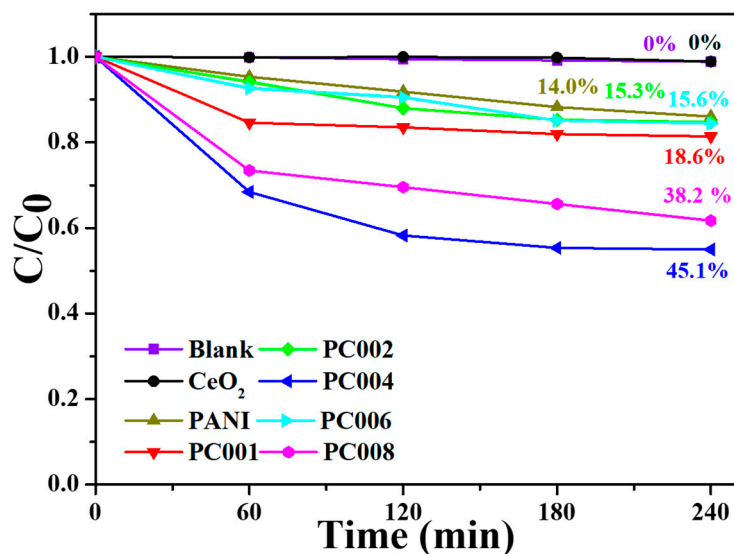


**Figure 9.** Photocatalytic MO degradation curve of the heterostructured CeO<sub>2</sub>/PANI powders under visible light irradiation as a function of the amount of PANI coating.

In order to investigate the recyclability of optimized photocatalysts, 4 wt % PANI-coated CeO<sub>2</sub> powder were used for four photocatalytic cycles of hydrogen production and MO degradation. After each photocatalytic reaction, the photocatalyst was separated, washed and dried, and used for further run without any treatment. Figure 10 shows the recycling tests of the PC004 photocatalyst for hydrogen production and MO degradation under visible light irradiation. For comparison with the data above, each cycle of hydrogen production and MO degradation lasted 6 h and 4 h, respectively. Note that both hydrogen production efficiency and MO degradation decreased as the cycle number increased. The hydrogen production efficiencies of the four cycles were 462.8, 371.2, 289.6, and 189.2  $\mu\text{mol g}^{-1}$  in sequence, while the MO degradation rates were 45.1%, 38.9%, 35.8%, and 33.7% in sequence, showing better stability of the photodegradation reaction. Compared with the first cycle, the hydrogen production efficiency was reduced by 60% after four cycles, while the MO degradation capability was only reduced by 25%. This is most likely attributed to the photocatalytic reaction between hydrogen production and MO degradation occurring at different sites on the catalyst surface. In addition, since PANI is an organic compound, radicals, generated by light irradiation, might induce PANI degradation [52], which may significantly decrease stability of the photocatalyst. Figure 11 shows the TGA (thermogravimetric analysis) curves of the PC004 before irradiation, after 6 h of hydrogen production and 4 h of MO degradation under visible light irradiation. Note that four different weight loss mechanisms took place in temperature ranges of 25°–150°, 150°–230°, 230°–440°, and 440°–530 °C. The first two weight losses were mainly attributed to water evaporation and elimination of impurities. The weight loss in temperature range 230–440 °C was attributed to the structural decomposition of the PANI and degradation of some oligomers [53], whereas the weight loss in temperature 440–530 °C was due to the loss of PANI main chain [54]. A comparison among the values at 150 °C, the weight losses of the sample before irradiation, after hydrogen production, and MO degradation were 3.9%, 6.8%, and 4.3%, respectively. The weight loss before irradiation was consistent with the amount of PANI coated in the composite powder, while the curves (b) and (c) of the composite powder after both photocatalytic reactions showed no significant PANI loss during the photocatalytic process. This indicates that the CeO<sub>2</sub>/PANI powder did not experience any significant PANI degradation during the photocatalytic reaction. However, the obvious increase in weight of curve (b) after the reaction does not exclude that it might be due to the complex reaction involved between the sacrificial reagent and the photocatalyst during hydrogen production, although the reaction mechanism remains unclear. The slight increase in weight of curve (c) was most likely due to the adsorption of a small amount of

organic substances during the MO degradation. These factors can mainly lead to a decrease in stability of the photocatalyst.

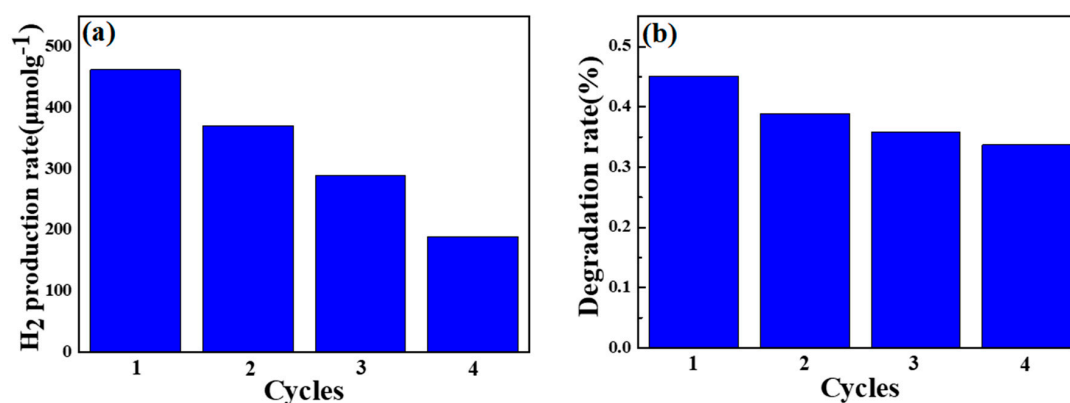


**Figure 10.** Recycling tests of the PC004 photocatalyst for (a) hydrogen production and (b) MO degradation under visible light irradiation.

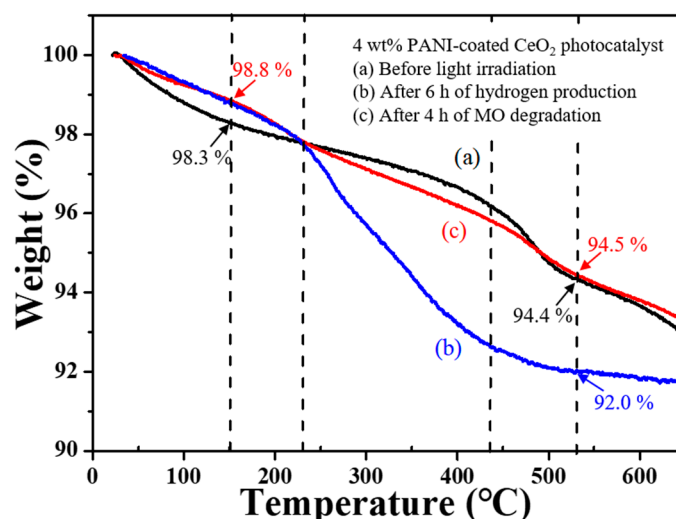


**Figure 11.** TGA curves of the PC004 photocatalyst (a) before light irradiation, (b) after 6-h of hydrogen production and (c) 4 h MO degradation under visible light irradiation.

Figure 12 shows a schematic diagram of the hydrogen production and MO degradation mechanisms of the CeO<sub>2</sub>/PANI powders under visible light irradiation. In the case of hydrogen production, in Figure 12a, when visible light irradiates the surface of a composite photocatalyst, the electrons of PANI are excited to transfer from the HOMO (highest occupied molecular orbital) to the LUMO (lowest unoccupied molecular orbital), leaving holes in the HOMO [55–57]. As seen in Figure 5, the PANI can absorb visible light and produce photogenerated electrons and holes under visible light irradiation in this system. Such electrons in LUMO will spontaneously transfer to the conduction band (CB) of CeO<sub>2</sub>, though CeO<sub>2</sub> cannot be excited by visible light. Such effect stimulates a more effective separation process of electron-hole pairs, which inhibits the recombination of charge carriers and enhances the photocatalytic activity. The photogenerated holes then decompose H<sub>2</sub>O into H<sup>+</sup> and OH<sup>-</sup>, and the electrons are combined with H<sup>+</sup> to produce H<sub>2</sub>. Furthermore, the MO degradation mechanism of the CeO<sub>2</sub>/PANI powders is shown in Figure 12b. In the same manner, the PANI with a closer HOMO-LUMO gap absorbs visible light to produce electron-hole pairs. The electrons are first excited from the HOMO to the LUMO and the holes are formed in the HOMO. The photogenerated electrons in LUMO then transfer to the CB of the CeO<sub>2</sub> catalyst and combine with oxygen (O<sub>2</sub>) to form superoxide anion radicals ( $\cdot\text{O}_2^-$ ). The holes in the HOMO will react with the hydroxide ions

(OH<sup>-</sup>) to form hydroxyl radicals ( $\cdot$ OH). Finally, although the gases released during the degradation process were not determined in this study, because MO is a quite complex molecule and may produce many other fragment ions, it has been demonstrated in literature that the MO can be decomposed into the products of gaseous dinitrogen, innocuous SO<sub>4</sub><sup>2-</sup> ions [58,59], water, and carbon dioxide [60] by the superoxide radicals (reductant) and the hydroxyl radicals (oxidant). Furthermore, according to the proposed mechanisms, the main reaction of MO degradation occurs on the surfaces of CeO<sub>2</sub> particle and PANI, while the reaction of hydrogen production only occurs on the surface of PANI. This suggests that when both surfaces of the CeO<sub>2</sub> and PANI are properly exposed, better photocatalytic properties can be obtained. Considering the recyclability results in Figure 10, this is a possible reason why the recyclability of MO degradation is better than that of hydrogen production. Therefore, although stability improvement remains challenging, in comparison with the uncoated CeO<sub>2</sub> powder, heterostructured CeO<sub>2</sub>/PANI composite powders with appropriate CeO<sub>2</sub>/PANI ratio, which have a relatively good photocatalytic performance under visible light irradiation, can generate hydrogen by water splitting and degrade MO, revealing it to be a potential material for photocatalytic applications.

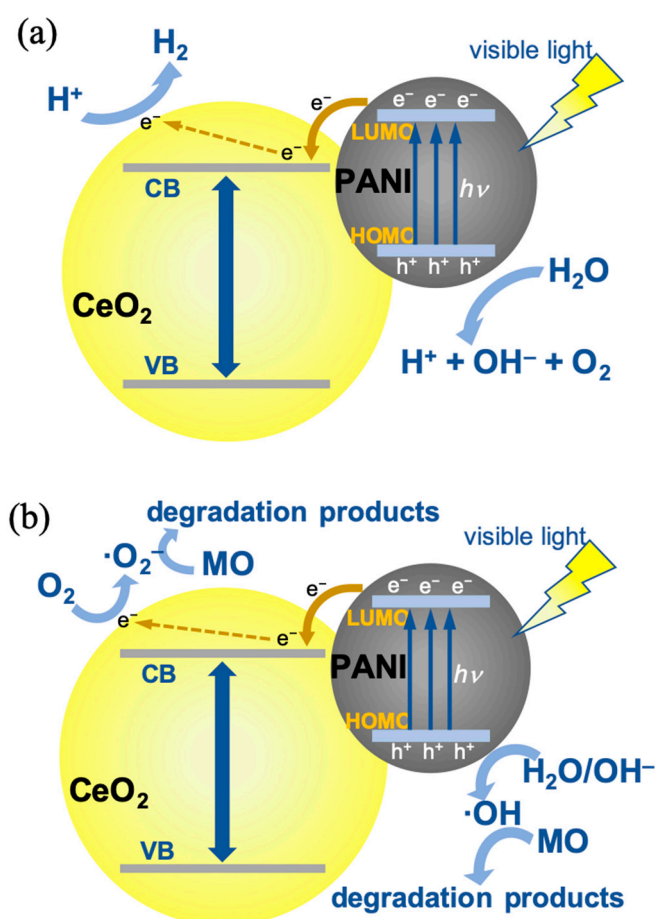


**Figure 12.** Schematic diagram of (a) hydrogen production and (b) MO degradation mechanisms of the heterostructured CeO<sub>2</sub>/PANI powders under visible light irradiation.

### 3. Material and Methods

#### 3.1. Materials

The following compounds were used: Ce(NO<sub>3</sub>)<sub>3</sub>·6H<sub>2</sub>O (Alfa Aesar, A Johnson Matthey Co., Haverhill, MA, USA), C<sub>6</sub>H<sub>7</sub>N (99.0% purity, Sigma Chemical Co., Saint Louis, MO, USA) and (NH<sub>4</sub>)<sub>2</sub>S<sub>2</sub>O<sub>8</sub>, (98% purity, Alfa Aesar, Haverhill, MA, USA), and further abbreviated in this report as

CeNH, ANI, and APS, respectively. The respective molecular weights of CeNH, ANI and APS reported by the manufacturers are 434.23, 93.13, and 228.19. The chemicals are all at reagent grades.

### 3.2. Materials Preparation

Ceria powder was homogeneously synthesized from the precursor cerium nitrate hydrate (CeNH) by the wet-chemical precipitation method [61]. Figure 13 shows the schematic diagram for the preparation of CeO<sub>2</sub>/PANI powder synthesized in this study. The concentration of precursor solution in de-ionized water was prepared at 5.0 wt %. After stirring and heating to 70 °C, aqueous ammonia was gradually added into the precursor solution to bring the pH value to ~8 for precipitation. After soaking at 70 °C for 1 h, the resulting suspension was cooled and stirred constantly at room temperature for 4 h to obtain precipitate. The precipitate was then rinsed several times and dried at 80 °C for 24 h. The as-dried powder was calcined at 500 °C for 2 h to obtain CeO<sub>2</sub> nanopowder for the following PANI deposition.

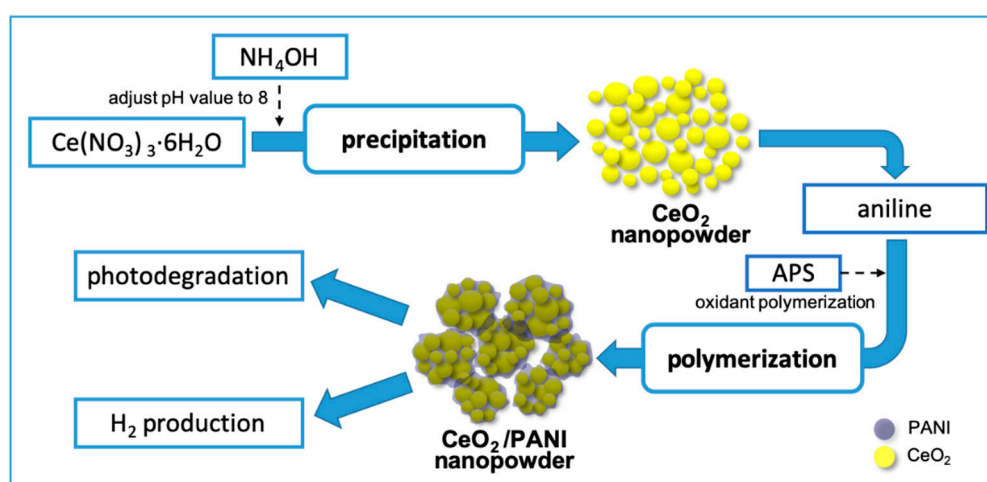


Figure 13. Schematic diagram for the preparation of CeO<sub>2</sub>/PANI powder.

Nanosized PANI was synthesized from an aqueous solution of aniline (ANI) on the surface of the CeO<sub>2</sub> particles with ammonium peroxydisulfate (APS) as an oxidant by polymerization [62]. Before deposition, the as-prepared CeO<sub>2</sub> powder was sufficiently mixed with hydrochloric acid (HCl, 1.0 M, 1.5 mL), APS (0.01 M) and deionized water (30 mL) by stirring for 1 h. Subsequently, ANI was added to the mixture in various concentrations by stirring at 15 °C for 8 h to complete the polymerization reaction. The resulting PANI-deposited CeO<sub>2</sub> powders were separated by centrifugation and rinsed repeatedly with deionized water and anhydrous alcohol several times. Finally, the products were dried at 80 °C for 24 h under vacuum. Moreover, CeO<sub>2</sub>/PANI powders were obtained with a PANI deposition amount of 1, 2, 4, 6, and 8 wt %, which were designated as PC001, PC002, PC004, PC006, and PC008, respectively.

### 3.3. Characterization of Photocatalysts

The morphological examination and nanostructural analysis of the synthesized CeO<sub>2</sub>/PANI powders were carried out using field-emission scanning electron microscopy (FE-SEM, JSM-7401F, JEOL, Tokyo, Japan) and transmission electron microscopy (TEM, 2100F, JEOL II, Tokyo, Japan), respectively. The phase identification was characterized by X-ray diffractometry (XRD, D8 Discover, Bruker, Karlsruhe, Germany). The specific surface area of the powders was determined by BET (Brunauer-Emmer-Teller) method from nitrogen adsorption/desorption isotherm data obtained at −196 °C on a constant-volume adsorption apparatus (SA-9600 Series, HORIBA, Tokyo, Japan). The structural information of the samples was measured by Fourier transform spectrophotometer (FTIR, FT-IR Spectrometer Frontier, Perkin Elmer, Waltham, MA, USA). The optical properties of the

powders were determined in the wavelength range of 300–800 nm using a UV-Vis absorption spectrum (Lambda 650S, PerkinElmer, Waltham, MA, USA) equipped with an integrating sphere attachment at room temperature. The photoluminescence (PL) spectra of the samples were measured at room temperature under 250 nm excitation wavelength (RF-5301-PC, Shimadzu, Tokyo, Japan). In the UV-Vis and PL tests, the powder was sandwiched between two pieces of glass for measurement. The weight loss of the CeO<sub>2</sub>/PANI powder before and after the photocatalytic reaction was determined using thermogravimetric analyzer (TGA, TGA2950, TA Instrument, New Castle, DE, USA) in the ambience conditions with the temperature ranging from 25 to 650 °C, and the heating rate at 10 °C/min.

#### 3.4. Measurement of Photocatalytic Activity

The photocatalytic activities of the CeO<sub>2</sub>/PANI composite powders were evaluated by degrading methylene orange (MO, C<sub>14</sub>H<sub>14</sub>N<sub>3</sub>NaO<sub>3</sub>S) under a visible light radiation system (HMLS-Xenon 300 W, HMT Co., Taiwan) with a UV-light blocking filter. The powder (0.1 g) was dispersed into an aqueous solution containing methylene orange (10 ppm, 100 mL). The distance between the visible light source and aqueous solution was set to 15 cm. The wavelength of the visible light source, xenon arc lamps with optical filtration (FEL0400, THORLABS Inc., Newton, NJ, USA), was in the range of 400–800 nm. Prior to visible light irradiation, the suspension was stirred in the dark for 30 min to reach adsorption–desorption equilibrium (set as “0 min”). During the illumination, individual samples were collected at 60-min intervals. The variation of the MO concentration, determined by the transmittance of the solution at 463 nm, was evaluated by UV-Vis spectrophotometry (U-2900, Hitachi, Tokyo, Japan). To avoid the effect of evaporation during illumination, the suspension was kept at a constant volume by adding water at 15-min intervals.

The photocatalytic water splitting of the CeO<sub>2</sub> powder with various amounts of PANI deposition was carried out in a Pyrex reaction vessel using visible light irradiation. Prior to photocatalysis reaction, argon gas was purged through the reactor to remove the dissolved oxygen. The photocatalysts were irradiated with the same illumination system as that in MO photodegradation (300 W Xe lamp) which allowed visible light to pass using a cut-off filter ( $\lambda \geq 400$  nm). The amount of hydrogen gas was determined using gas chromatography (GC-2014, Shimadzu, Tokyo, Japan) equipped with a thermal conductivity detector (TCD).

## 4. Conclusions

Heterostructured CeO<sub>2</sub>/PANI powder was successfully prepared by precipitation and followed polymerization as a function of the amount of PANI coating. The structural analysis confirmed that the obtained composite powder exhibited a cubic fluorite structure with a particle size of ca. 25–40 nm, showing a tendency of agglomeration with the increase in PANI coating. With the optimal coating amount of 4 wt % PANI, the photocatalytic efficiency of the CeO<sub>2</sub> powder can be significantly increased from a non-catalytic state to a MO degradation of 45% within 4 h and a hydrogen production of 462  $\mu\text{mol g}^{-1}$  within 6 h under visible light irradiation. The heterostructured CeO<sub>2</sub>/PANI powder with appropriate CeO<sub>2</sub>/PANI ratio is thus considered as one of the potential visible light-driven photocatalysts.

**Author Contributions:** Conceptualization, C.-Y.C.; methodology, Y.-S.L. and C.-Y.C.; formal analysis, Y.-S.L. and G.-J.L.; investigation, Y.-S.L. and G.-J.L.; resources, J.J.W., Y.-C.C., C.-Y.T., J.-H.C., T.-L.H., and C.-Y.C.; writing—original draft preparation, Y.-S.L., C.-Y.C., and A.F.; writing—review and editing, C.-Y.C. and A.F.; supervision, C.-Y.C.; project administration, Y.-S.L. and G.-J.L.; funding acquisition, J.J.W., Y.-C.C., C.-Y.T., J.-H.C., T.-L.H., and C.-Y.C. All authors have read and agreed to the published version of the manuscript.

**Funding:** This research was funded by the Ministry of Science and Technology of Taiwan Grant Nos. MOST 108-2918-I-035-004, 107-2218-E-035-010, and 106-2221-E-035-035-MY2.

**Acknowledgments:** The authors would like to thank the Ministry of Science and Technology of Taiwan for financially supporting this work. The authors also appreciate the Precision Instrument Support Center of Feng Chia University in providing the measurement facilities.

**Conflicts of Interest:** The authors declare no conflict of interest.

## References

1. Qu, Y.; Duan, X. Progress, challenge and perspective of heterogeneous photocatalysts. *Chem. Soc. Rev.* **2013**, *42*, 2568–2580. [[CrossRef](#)] [[PubMed](#)]
2. Chouhan, N.; Meena, R.K.; Liu, R.-S. Chapter 8: Hydrogen. In *An Alternative Fuel, Solar Energy Conversion and Storage: Some Photochemical Modes*; Ameta, S.C., Ameta, R., Eds.; Taylor & Francis Group: Oxfordshire, UK; CRC Press: Boca Raton, FL, USA, 2015.
3. Kamat, P.V. Meeting the clean energy demand: Nanostructure architectures for solar energy conversion. *J. Phys. Chem. C* **2007**, *111*, 2834–2860. [[CrossRef](#)]
4. Kudo, A.; Miseki, Y. Heterogeneous photocatalyst materials for water splitting. *Chem. Soc. Rev.* **2009**, *38*, 253–278. [[CrossRef](#)] [[PubMed](#)]
5. Hoffmann, M.R.; Martin, S.T.; Choi, W.; Bahnemann, D.W. Environmental applications of semiconductor photocatalysis. *Chem. Rev.* **1995**, *95*, 69–96. [[CrossRef](#)]
6. Tuprakay, S.; Liengcharernsit, W. Lifetime and regeneration of immobilized titania for photocatalytic removal of aqueous hexavalent chromium. *J. Hazard. Mater.* **2005**, *124*, 53–58. [[CrossRef](#)]
7. López, A.; Acosta, D.; Mtz-Enriquez, A.; Santiago, J. Nanostructured low crystallized titanium dioxide thin films with good photocatalytic activity. *Powder Technol.* **2010**, *202*, 111–117. [[CrossRef](#)]
8. Chin, S.; Park, E.; Kim, M.; Jurng, J. Photocatalytic degradation of methylene blue with TiO<sub>2</sub> nanoparticles prepared by a thermal decomposition process. *Powder Technol.* **2010**, *201*, 171–176. [[CrossRef](#)]
9. Choudhury, B.; Chetri, P.; Choudhury, A. Oxygen defects and formation of Ce<sup>3+</sup> affecting the photocatalytic performance of CeO<sub>2</sub> nanoparticles. *RSC Adv.* **2014**, *4*, 4663–4671. [[CrossRef](#)]
10. Liu, H.; Wang, M.; Wang, Y.; Liang, Y.; Cao, W.; Su, Y. Ionic liquid-templated synthesis of mesoporous CeO<sub>2</sub>-TiO<sub>2</sub> nanoparticles and their enhanced photocatalytic activities under UV or visible light. *J. Photochem. Photobiol. A Chem.* **2011**, *223*, 157–164. [[CrossRef](#)]
11. Zhai, Y.; Zhang, S.; Pang, H. Preparation, characterization and photocatalytic activity of CeO<sub>2</sub> nanocrystalline using ammonium bicarbonate as precipitant. *Mater. Lett.* **2007**, *61*, 1863–1866. [[CrossRef](#)]
12. Ebadi, M.; Amiri, O.; Sabet, M. Synthesis of CeO<sub>2</sub>/Au/Ho nanostructures as novel and highly efficient visible light driven photocatalyst. *Sep. Purif. Technol.* **2018**, *190*, 117–122. [[CrossRef](#)]
13. Chai, S.Y.; Kim, Y.J.; Jung, M.H.; Chakraborty, A.K.; Jung, D.; Lee, W.I. Heterojunctioned BiOCl/Bi<sub>2</sub>O<sub>3</sub>, a new visible light photocatalyst. *J. Catal.* **2009**, *262*, 144–149. [[CrossRef](#)]
14. Sun, C.; Li, H.; Chen, L. Nanostructured ceria-based materials: Synthesis, properties, and applications. *Energy Environ. Sci.* **2012**, *5*, 8475–8505. [[CrossRef](#)]
15. Chaudhary, Y.S.; Panigrahi, S.; Nayak, S.; Satpati, B.; Bhattacharjee, S.; Kulkarni, N. Facile synthesis of ultra-small monodisperse ceria nanocrystals at room temperature and their catalytic activity under visible light. *J. Mater. Chem.* **2010**, *20*, 2381–2385. [[CrossRef](#)]
16. Kominami, H.; Tanaka, A.; Hashimoto, K. Mineralization of organic acids in aqueous suspensions of gold nanoparticles supported on cerium (iv) oxide powder under visible light irradiation. *Chem. Commun.* **2010**, *46*, 1287–1289. [[CrossRef](#)] [[PubMed](#)]
17. Primo, A.; Marino, T.; Corma, A.; Molinari, R.; García, H. Efficient visible-light photocatalytic water splitting by minute amounts of gold supported on nanoparticulate CeO<sub>2</sub> obtained by a biopolymer templating method. *J. Am. Chem. Soc.* **2011**, *133*, 6930–6933. [[CrossRef](#)] [[PubMed](#)]
18. Arul, N.S.; Mangalaraj, D.; Ramachandran, R.; Gracec, A.N.; Han, J.I. Fabrication of CeO<sub>2</sub>/Fe<sub>2</sub>O<sub>3</sub> composite nanospindles for enhanced visible light driven photocatalysts and supercapacitor electrodes. *J. Mater. Chem. A* **2015**, *3*, 15248–15258. [[CrossRef](#)]
19. Syazwani, O.N.; Hir, Z.A.M.; Mukhair, H.; Mastuli, M.S.; Abdullah, A.H. Designing visible-light-driven photocatalyst of Ag<sub>3</sub>PO<sub>4</sub>/CeO<sub>2</sub> for enhanced photocatalytic activity under low light irradiation. *J. Mater. Sci. Mater. Electron.* **2019**, *30*, 415–423. [[CrossRef](#)]
20. Wang, L.; Ding, J.; Chai, Y.; Liu, Q.; Ren, J.; Liu, X.; Dai, W.-L. CeO<sub>2</sub> nanorod/g-C<sub>3</sub>N<sub>4</sub>/N-rGO composite: Enhanced visible-light-driven photocatalytic performance and the role of N-rGO as electronic transfer media. *Dalton Trans.* **2015**, *44*, 11223–11234. [[CrossRef](#)]

21. Khan, M.M.; Ansari, S.A.; Pradhan, D.; Han, D.H.; Lee, J.; Cho, M.H. Defect-induced band gap narrowed CeO<sub>2</sub> nanostructures for visible light activities. *Ind. Eng. Chem. Res.* **2014**, *53*, 9754–9763. [[CrossRef](#)]
22. Saravanan, R.; Agarwal, S.; Gupta, V.K.; Khan, M.M.; Gracia, F.; Mosquera, E.; Narayanan, V.; Stephen, A. Line defect Ce<sup>3+</sup> induced Ag/CeO<sub>2</sub>/ZnO nanostructure for visible-light photocatalytic activity. *J. Photochem. Photobiol. A* **2018**, *353*, 499–506. [[CrossRef](#)]
23. Bhadra, S.; Khastgir, D.; Singha, N.K.; Lee, J.H. Progress in preparation, processing and applications of polyaniline. *Prog. Polym. Sci.* **2009**, *34*, 783–810. [[CrossRef](#)]
24. Eftekhari, A.; Li, L.; Yang, Y. Polyaniline supercapacitors. *J. Power Sources* **2017**, *347*, 86–107. [[CrossRef](#)]
25. Bogdanović, U.; Pašti, I.; Ćirić-Marjanović, G.; Mitrić, M.; Ahrenkiel, S.P.; Vodnik, V. Interfacial synthesis of gold-polyaniline nanocomposite and its electrocatalytic application. *ACS Appl. Mater. Interfaces* **2015**, *7*, 28393–28403. [[CrossRef](#)]
26. Sharma, A.; Tomar, M.; Gupta, V.; Badola, A.; Goswami, N. Polyaniline/SnO<sub>2</sub> nanocomposite sensor for NO<sub>2</sub> gas sensing at low operating temperature. *Int. J. Nanosci.* **2015**, *14*, 1550011. [[CrossRef](#)]
27. Sharma, H.J.; Salorkar, M.A.; Kondawar, S.B. H<sub>2</sub> and CO gas sensor from SnO<sub>2</sub>/polyaniline composite nanofibers fabricated by electrospinning. *Adv. Mater. Proc.* **2017**, *2*, 61–66. [[CrossRef](#)]
28. Gao, J.; Li, S.; Yang, W.; Zhao, G.; Bo, L.; Song, L. Preparation and photocatalytic activity of PANI/TiO<sub>2</sub> composite film. *Rare Met.* **2007**, *26*, 1–7. [[CrossRef](#)]
29. Zhang, H.; Zong, R.; Zhao, J.; Zhu, Y. Dramatic visible photocatalytic degradation performances due to synergetic effect of TiO<sub>2</sub> with PANI. *Environ. Sci. Technol.* **2008**, *42*, 3803–3807. [[CrossRef](#)]
30. Salem, M.A.; Al-Ghonemiy, A.F.; Zaki, A.B. Photocatalytic degradation of Allura red and Quinoline yellow with Polyaniline/TiO<sub>2</sub> nanocomposite. *Appl. Catal. B Environ.* **2009**, *91*, 59–66. [[CrossRef](#)]
31. Wang, Q.; Hui, J.; Li, J.; Cai, Y.; Yin, S.; Wang, F.; Su, B. Photodegradation of methyl orange with PANI-modified BiOCl photocatalyst under visible light irradiation. *Appl. Surf. Sci.* **2013**, *283*, 577–583. [[CrossRef](#)]
32. Lafuente, E.; Callejas, M.; Sainz, R.; Benito, A.M.; Maser, W.; Sanjuán, M.; Saurel, D.; De Teresa, J.M.; Martínez, M.T. The influence of single-walled carbon nanotube functionalization on the electronic properties of their polyaniline composites. *Carbon* **2008**, *46*, 1909–1917. [[CrossRef](#)]
33. Jiménez, P.; Castell, P.; Sainz, R.; Ansón, A.; Martínez, M.T.; Benito, A.M.; Maser, W.K. Carbon nanotube effect on polyaniline morphology in water dispersible composites. *J. Phys. Chem. B* **2010**, *114*, 1579–1585. [[CrossRef](#)] [[PubMed](#)]
34. Reddy, K.R.; Karthik, K.; Prasad, S.B.; Soni, S.K.; Jeong, H.M.; Raghu, A.V. Enhanced photocatalytic activity of nanostructured titanium dioxide/polyaniline hybrid photocatalysts. *Polyhedron* **2016**, *120*, 169–174. [[CrossRef](#)]
35. Saravanan, R.; Sacari, E.J.S.; Gracia, F.; Khan, M.M.; Mosquera, E.; Gupta, V.K. Conducting PANI stimulated ZnO system for visible light photocatalytic degradation of coloured dyes. *J. Mol. Liq.* **2016**, *221*, 1029–1033. [[CrossRef](#)]
36. Kumar, E.; Selvarajan, P.; Muthuraj, D. Preparation and characterization of polyaniline/cerium dioxide (CeO<sub>2</sub>) nanocomposite via in situ polymerization. *J. Mater. Sci.* **2012**, *47*, 7148–7156. [[CrossRef](#)]
37. Samai, B.; Bhattacharya, S.C. Conducting polymer supported cerium oxide nanoparticle: Enhanced photocatalytic activity for waste water treatment. *Mater. Chem. Phys.* **2018**, *220*, 171–181. [[CrossRef](#)]
38. Vidya, J.; Balamurugan, P. Photocatalytic degradation of Methylene Blue using PANi/Ceria nanocomposite under visible light irradiation. *Desalin. Water Treat.* **2019**, *156*, 349–356. [[CrossRef](#)]
39. Choudhury, B.; Choudhury, A. Ce<sup>3+</sup> and oxygen vacancy mediated tuning of structural and optical properties of CeO<sub>2</sub> nanoparticles. *Mater. Chem. Phys.* **2012**, *131*, 666–671. [[CrossRef](#)]
40. You, D.; Pan, B.; Jiang, F.; Zhou, Y.; Su, W. CdS nanoparticles/CeO<sub>2</sub> nanorods composite with high-efficiency visible-light-driven photocatalytic activity. *Appl. Surf. Sci.* **2016**, *363*, 154–160. [[CrossRef](#)]
41. Mani, A.D.; Nandy, S.; Subrahmanyam, C. Synthesis of CdS/CeO<sub>2</sub> nanomaterials for photocatalytic H<sub>2</sub> production and simultaneous removal of phenol and Cr(VI). *J. Environ. Chem. Eng.* **2015**, *3*, 2350–2357. [[CrossRef](#)]
42. Saravanan, S.; Mathai, C.J.; Anantharaman, M.; Venkatachalam, S.; Prabhakaran, P. Investigations on the electrical and structural properties of polyaniline doped with camphor sulphonic acid. *J. Phys. Chem. Solids* **2006**, *67*, 1496–1501. [[CrossRef](#)]
43. Babu, V.J.; Vempati, S.; Ramakrishna, S. Conducting polyaniline-electrical charge transportation. *Mater. Sci. Appl.* **2013**, *4*, 1–10. [[CrossRef](#)]

44. Jian, K.-S.; Chang, C.-J.; Wu, J.J.; Chang, Y.-C.; Tsay, C.-Y.; Chen, J.-H.; Horng, T.-L.; Lee, G.-J.; Karupphasamy, L.; Anandan, S.; et al. High response CO sensor based on a polyaniline/SnO<sub>2</sub> Nanocomposite. *Polymers* **2019**, *11*, 184. [CrossRef]
45. Jamal, R.; Xu, F.; Shao, W.; Abdiryim, T. The study on the application of solid-state method for synthesizing the polyaniline/noble metal (Au or Pt) hybrid materials. *Nanoscale Res. Lett.* **2013**, *8*, 117. [CrossRef]
46. Wang, C.; Wang, L.; Jin, J.; Liu, J.; Li, Y.; Wu, M.; Chen, L.; Wang, B.; Yang, X.-Y.; Su, B.-L. Probing effective photocorrosion inhibition and highly improved photocatalytic hydrogen production on monodisperse PANI@CdS core-shell nanospheres. *Appl. Catal. B Environ.* **2016**, *188*, 351–359. [CrossRef]
47. Kumaravel, V.; Imam, M.D.; Badreldin, A.; Chava, R.K.; Do, J.Y.; Kang, M.; Abdel-Wahab, A. Photocatalytic hydrogen production: Role of sacrificial reagents on the activity of oxide, carbon, and sulfide catalysts. *Catalysts* **2019**, *9*, 276. [CrossRef]
48. López, C.R.; Melián, E.P.; Méndez, J.O.; Santiago, D.E.; Rodríguez, J.M.D.; Díaz, O.M.G. Comparative study of alcohols as sacrificial agents in H<sub>2</sub> production by heterogeneous photocatalysis using Pt/TiO<sub>2</sub> catalysts. *J. Photochem. Photobiol. A Chem.* **2015**, *312*, 45–54. [CrossRef]
49. Yu, W.J.; Cheng, Y.; Zou, T.; Liu, Y.; Wu, K.; Peng, N. Preparation of BiPO<sub>4</sub>-polyaniline hybrid and its enhanced photocatalytic performance. *Nano* **2018**, *13*, 1850009. [CrossRef]
50. Yan, C.; Zhang, Z.; Wang, W.; Ju, T.; She, H.; Wang, Q. Synthesis and characterization of polyaniline-modified BiOI: A visible-light-response photocatalyst. *J. Mater. Sci. Mater. Electron.* **2018**, *29*, 18343–18351. [CrossRef]
51. Hao, X.; Gong, J.; Ren, L.; Zhang, D.; Xiao, X.; Jiang, Y.; Zhang, F.; Tong, Z. Preparation of polyaniline modified BiOBr with enhanced photocatalytic activities. *Funct. Mater. Lett.* **2017**, *10*, 1750040. [CrossRef]
52. Gilja, V.; Novaković, K.; Trivas-Sejdic, J.; Hrnjak-Murgić, Z.; Roković, M.K.; Žic, M. Stability and synergistic effect of polyaniline/TiO<sub>2</sub> photocatalysts in degradation of azo dye in wastewater. *Nanomaterials* **2017**, *7*, 412. [CrossRef] [PubMed]
53. Kim, B.-J.; Oh, S.-G.; Han, M.G.; Im, S.-S. Synthesis and characterization of polyaniline nanoparticles in SDS micellar solutions. *Synth. Met.* **2001**, *122*, 297–304. [CrossRef]
54. Sambaza, S.; Maity, A.; Pillay, K. Enhanced degradation of BPA in water by PANI supported Ag/TiO<sub>2</sub> nanocomposite under UV and visible light. *J. Environ. Chem. Eng.* **2019**, *7*, 102880. [CrossRef]
55. Hidalgo, D.; Bocchini, S.; Fontana, M.; Saracco, G.; Hernández, S. Green and low-cost synthesis of PANI-TiO<sub>2</sub> nanocomposite mesoporous films for photoelectrochemical water splitting. *RSC Adv.* **2015**, *5*, 49429–49438. [CrossRef]
56. Tang, Y.; Zhou, P.; Wang, K.; Lin, F.; Lai, J.; Chao, Y.; Li, H.; Guo, S. BiOCl/ultrathin polyaniline core/shell nanosheets with a sensitization mechanism for efficient visible-light-driven photocatalysis. *Sci. China Mater.* **2018**, *62*, 95–102. [CrossRef]
57. Lee, S.L.; Chang, C.-J. Recent developments about conductive polymer based composite photocatalysts. *Polymers* **2019**, *11*, 206. [CrossRef]
58. Lei, Y.; Wang, G.; Song, S.; Fan, W.; Pang, M.; Tang, J.; Zhang, H. Room temperature, template-free synthesis of BiOI hierarchical structures: Visible-light photocatalytic and electrochemical hydrogen storage properties. *Dalton Trans.* **2010**, *39*, 3273–3278. [CrossRef]
59. Lachheb, H.; Puzenat, E.; Houas, A.; Ksibi, M.; Elaloui, E.; Guillard, C.; Herrmann, J.-M. Photocatalytic degradation of various types of dyes (Alizarin S, Crocein Orange G, Methyl Red, Congo Red, Methylene Blue) in water by UV-irradiated titania. *Appl. Catal. B Environ.* **2002**, *39*, 75–90. [CrossRef]
60. Li, J.; Xiao, Q.; Li, L.; Shen, J.; Hu, D. Novel ternary composites: Preparation, performance and application of ZnFe<sub>2</sub>O<sub>4</sub>/TiO<sub>2</sub>/polyaniline. *Appl. Surf. Sci.* **2015**, *331*, 108–114. [CrossRef]
61. Chen, C.-Y.; Chang, K.-H. Temperature independent resistive oxygen sensor prepared using zirconia-doped ceria powders. *Sens. Actuators B Chem.* **2012**, *162*, 68–75. [CrossRef]
62. Zhang, Y.; Dou, C.; Wang, W.; Feng, N. Synthesis of uniform polyaniline nanosheets and nanotubes: Dependence of morphology on the pH. *Macromol. Res.* **2016**, *24*, 663–669. [CrossRef]

